

Modulating adsorbed hydrogen drives electrochemical CO₂-to-C₂ products

Received: 1 November 2022

Accepted: 26 July 2023

Published online: 01 August 2023

Check for updates

Jiaqi Feng¹, Libing Zhang ^{1,2}, Shoujie Liu ³, Liang Xu¹, Xiaodong Ma^{1,2}, Xingxing Tan^{1,2}, Limin Wu^{1,2}, Qingli Qian ^{1,2}, Tianbin Wu^{1,2}, Jianling Zhang^{1,2}, Xiaofu Sun ^{1,2} ✉ & Buxing Han ^{1,2,4} ✉

Electrocatalytic CO₂ reduction is a typical reaction involving two reactants (CO₂ and H₂O). However, the role of H₂O dissociation, which provides active *H species to multiple protonation steps, is usually overlooked. Herein, we construct a dual-active sites catalyst comprising atomic Cu sites and Cu nanoparticles supported on N-doped carbon matrix. Efficient electrosynthesis of multi-carbon products is achieved with Faradaic efficiency approaching 75.4% with a partial current density of 289.2 mA cm⁻² at -0.6 V. Experimental and theoretical studies reveal that Cu nanoparticles facilitate the C-C coupling step through *CHO dimerization, while the atomic Cu sites boost H₂O dissociation to form *H. The generated *H migrate to Cu nanoparticles and modulate the *H coverage on Cu NPs, and thus promote *CO-to-*CHO. The dual-active sites effect of Cu single-sites and Cu nanoparticles gives rise to the catalytic performance.

Heterogeneous catalysis holds great promise for practical applications in both the petrochemical and fine chemical industries, primarily due to its ease of catalyst separation and recovery^{1,2}. However, it remains challenging when two or multiple reactants coexist in the system. To achieve satisfactory catalytic performance, dual-/multi- active sites catalysts have attracted great attention recently^{3,4}. These catalysts possess multiple active sites that endow them with improved catalytic properties, enabling the activation of two or more reactants, which provide more efficient reaction pathway and accelerate the entire reaction, leading to the significantly enhanced activity and selectivity for the target products.

As one of the representative reactions that involves two reactants (CO₂ and H₂O) and multiple protonation steps, the electrocatalytic CO₂ reduction reaction (CO₂RR) to chemicals and fuels offers a promising route to store renewable energy and manage the global carbon balance⁵⁻⁸. Substantial efforts have been dedicated to developing dual-active sites catalysts to enhance CO₂RR performance. Many reported catalysts consist of active sites responsible for CO₂ activation (e.g., Au,

Ag and Zn) and further hydrogenation or C-C coupling (Cu). It has been demonstrated that the intermediate migration (e.g., *CO) plays a crucial role on the selectivity of the reaction, which greatly influenced by the optimal distribution and distance between the dual active sites. Meanwhile, an increase in the *CO coverage over Cu sites has been shown to promote the formation of C₂₊ products⁹⁻¹¹. In addition, considering H₂O molecule serves as the proton source for hydrogenation step, the active site for H₂O dissociation has been designed to be part of the dual-active sites catalysts^{12,13}. The introduction of H₂O dissociation sites, such as metal single atoms, sulfur, and oxygen vacancies, has been demonstrated to accelerate the rate of H₂O dissociation into *H species, which are subsequently fed to CO₂ conversion sites through *H spillover¹⁴⁻¹⁶. However, the existing findings have mainly focused on the influence of H₂O dissociation in CO₂-to-C₁ product process (formate or methane), while it is of greater significance for the C₂ products formation process. This is due to the commonly used alkaline electrolyte in CO₂-to-C₂ product, which slows down the H₂O dissociation step, resulting in a sluggish reaction kinetic

¹Beijing National Laboratory for Molecular Sciences, Key Laboratory of Colloid and Interface and Thermodynamics, Center for Carbon Neutral Chemistry, Institute of Chemistry, Chinese Academy of Sciences, Beijing 100190, China. ²School of Chemical Sciences, University of Chinese Academy of Sciences, Beijing 100049, China. ³School of Materials Science and Engineering, Anhui University, Hefei 230601, China. ⁴Shanghai Key Laboratory of Green Chemistry and Chemical Processes, School of Chemistry and Molecular Engineering, East China Normal University, Shanghai 200062, China.

✉ e-mail: sunxiaofu@iccas.ac.cn; hanbx@iccas.ac.cn

process^{15,17}. Therefore, the constructing dual-active sites electrocatalyst to accelerate CO₂ reduction and H₂O dissociation respectively is a feasible strategy for achieving the desired electrochemical CO₂-to-C₂ products performance.

Cu is the most promising electrocatalyst for converting CO₂ into C₂ products, owing to its moderate adsorption capacity for key intermediates^{18–20}. Various strategies have been investigated to improve the C₂ selectivity and current density, such as the manipulation of crystal facets, morphology, particle size, and oxidation state^{21–23}. However, most of these studies mainly focus on regulating the Cu structure for CO₂ activation and C-C coupling, with limited reports on the impact of surface *H coverage through accelerated H₂O dissociation. It is crucial to carefully control the coverage of *H species since an excessive amount promotes H₂ production through the competing hydrogen evolution reaction (HER). Recently, single-atom catalysts, characterized by the uniform dispersion of isolated metal atoms on a substrate, have received significant attention in the field of HER due to their high metal utilization, tunable electronic structures and structural stability. Notably, the HER activity of single-atom Cu catalyst in alkaline electrolyte can be regulated through modifying coordinated environment and support type^{24–26}. Therefore, designing of a dual-active sites catalyst incorporating co-loaded Cu nanoparticles (NPs) and single-atom Cu sites offers the potential for simultaneous CO₂ conversion and H₂O activation, favoring the high-performance for electroproduction of C₂ products.

Herein, we have constructed a dual-active sites catalyst containing moderate content ratio (0.25) of atomic Cu sites to Cu NPs (M-Cu₁/Cu_{NP}) for CO₂ electroreduction to C₂ products. The M-Cu₁/Cu_{NP} exhibited a high C₂ products Faradaic efficiency (FE_{C2}) of 75.4% with corresponding a partial current density of C₂ products (*j*_{C2}) of 289.2 mA cm⁻² at -0.6 V versus reversible hydrogen electrode (*vs.* RHE, all potentials are referenced to RHE). Moreover, the stable CO₂-to-C₂ products conversion with FEs of >70% can maintain at a constant current density of 400 mA cm⁻² for a run time of 40 h. The experiments and density functional theory (DFT) calculations revealed that Cu NPs facilitated CO₂ activation, *CO hydrogenation into *CHO, and C-C coupling into C₂ products. The atomic Cu site accelerated H₂O dissociation to provide *H, and the generated *H transferred to Cu NPs through N-doped carbon matrix and modulated the *H coverage on Cu NPs, which reduced the energy barrier for *CO to *CHO.

Results

Synthesis and characterization of M-Cu₁/Cu_{NP} catalyst

The M-Cu₁/Cu_{NP} catalyst was synthesized through a facile pyrolysis strategy by calcining Cu complexes in Ar flow and then reducing in H₂ flow. The Cu complexes were obtained by mixing Cu(NO₃)₂·3H₂O and guanidine thiocyanate with a 1:8 mole ratio in deionized water and subsequently evaporating the solvent. By varying the amount of Cu(NO₃)₂·3H₂O, the catalysts containing the rich (R-Cu₁/Cu_{NP}) and poor (P-Cu₁/Cu_{NP}) amount of Cu₁ site were also prepared using the same procedure. The morphology of the as-prepared catalyst was characterized by transmission electron microscopy (TEM). The dark-field TEM image (Fig. 1a) shows that obvious nanoparticles with the average size of ~4 nm are uniformly dispersed on carbon matrix in M-Cu₁/Cu_{NP}. The corresponding high-resolution (HR) TEM image of the nanoparticle displays the distinct lattice fringes with an interplanar space of 0.208 nm, consistent with the (111) plane of metallic Cu (Fig. 1b), confirming the uniformly dispersed nanoparticles are Cu NPs. The dispersion of atomic Cu was then identified by the aberration-corrected high-angle annular dark-field scanning transmission electron microscopy (HAADF-STEM). As presented in Fig. 1c, the isolated bright dots can be recognized as well distributed Cu atoms in M-Cu₁/Cu_{NP}, which have been highlighted by red circles. The energy-dispersive X-ray spectroscopy (EDS) elemental mapping images (Fig. 1d) reveal a uniform distribution of C, N and Cu, indicating that

they are homogeneous over the entire architectures. Therefore, we can conclude that a dual-active sites catalyst containing atomically dispersed Cu sites adjacent to uniformly dispersed Cu NPs was successfully prepared. In addition, the TEM and aberration-corrected HAADF-STEM images of P-Cu₁/Cu_{NP} and R-Cu₁/Cu_{NP} are shown in Fig. S1 and Fig. S2, respectively. The TEM images showed that both P-Cu₁/Cu_{NP} and R-Cu₁/Cu_{NP} exhibited a similar average size of Cu NPs compared to M-Cu₁/Cu_{NP}, while the amount of Cu NPs obviously decreased over R-Cu₁/Cu_{NP}. Meanwhile, evident single atomic Cu can also be observed on HAADF-STEM images of P-Cu₁/Cu_{NP} and R-Cu₁/Cu_{NP}. The X-ray diffraction (XRD) patterns of P-Cu₁/Cu_{NP}, M-Cu₁/Cu_{NP} and R-Cu₁/Cu_{NP} in Fig. 1e show that only the characteristic peaks of metallic Cu and carbon were observed, and the strong peak at 43.2° can be assigned to Cu(111) facet, which is consistent with the HRTEM results. The X-ray photoelectron spectroscopy (XPS) survey spectra show that the presence of Cu, N, C and O elements in P-Cu₁/Cu_{NP}, M-Cu₁/Cu_{NP} and R-Cu₁/Cu_{NP} (Fig. S3), where the existence of O element can be attributed to the adsorbed oxygen on surface. The Cu content in P-Cu₁/Cu_{NP}, M-Cu₁/Cu_{NP}, and R-Cu₁/Cu_{NP} was determined to be 7.4, 4.3, and 1.9 at%, respectively, and the corresponding N and C content are displayed in Table S1. The Cu 2*p* spectra (Fig. 1f) suggest that only Cu 2*p*_{3/2} peak attributed to Cu^{0/+} existed in the spectra, which moved to lower binding energy in the order of R-Cu₁/Cu_{NP} (933.0 eV), M-Cu₁/Cu_{NP} (932.7 eV) and P-Cu₁/Cu_{NP} (932.5 eV), indicating a gradual increase in the valence state of Cu in the catalysts. The Cu LMM Auger spectra confirmed the coexistence of Cu⁺ and Cu⁰ in P-Cu₁/Cu_{NP}, M-Cu₁/Cu_{NP} and R-Cu₁/Cu_{NP} (Fig. S4). Considering that the valence state of Cu in Cu NP is 0, while that of atomically dispersed Cu site is Cu^{δ+}, the content of Cu₁ site in the catalyst changed in order of P-Cu₁/Cu_{NP} < M-Cu₁/Cu_{NP} < R-Cu₁/Cu_{NP}. Meanwhile, the high resolution XPS N 1*s* spectra of P-Cu₁/Cu_{NP}, M-Cu₁/Cu_{NP}, and R-Cu₁/Cu_{NP} are displayed in Fig. S5. All spectra showed obvious Cu-N peak at around 399.2 eV, which suggests that the Cu₁ sites were coordinated by N atoms and other peaks could be attributed to pyridinic N (-398.5 eV), pyrrolic N (-399.9 eV), and graphitic (-401.0 eV), respectively.

To further determine the chemical state and local coordination environment, X-ray absorption near-edge structure (XANES) and extended X-ray absorption fine structure (EXAFS) measurements were conducted. The Cu K-edge XANES of R-Cu₁/Cu_{NP}, M-Cu₁/Cu_{NP} and P-Cu₁/Cu_{NP} with the reference samples Cu foil and Cu phthalocyanine (Cu Pc) were presented in Fig. 1g, the adsorption edge of all catalysts located between that of Cu foil and Cu Pc, indicating the average Cu valence state of Cu in the catalysts laid between 0 and +2. Meanwhile, the adsorption edge shifted to higher energy in the sequence of P-Cu₁/Cu_{NP} < M-Cu₁/Cu_{NP} < R-Cu₁/Cu_{NP}, confirming that the average Cu valence state increased with the increase in the Cu₁/Cu_{NP} ratio. It is in accordance with the XPS results. The Fourier-transformed (FT) EXAFS spectra in the R-space of the three catalysts were processed and displayed in Fig. 1h, all three catalysts exhibited peaks at around 1.5 Å and 2.2 Å, attributed to Cu-N and Cu-Cu coordination, respectively. Therefore, both atomic Cu and metallic Cu NP coexisted in R-Cu₁/Cu_{NP}, M-Cu₁/Cu_{NP} and P-Cu₁/Cu_{NP}. Notably, the intensity ratio of the Cu-N peak to the Cu-Cu peak increased in the order of P-Cu₁/Cu_{NP} < M-Cu₁/Cu_{NP} < R-Cu₁/Cu_{NP}, indicating a gradual increase in the content ratio of atomic Cu to Cu NP. In order to obtain the local structure of Cu species and the content ratio of atomic Cu to Cu NP, the quantitative analysis by the least-squares EXAFS fittings was performed (Fig. S6). The percentages (P) of Cu-N₄ (Cu₁) and Cu NPs in total Cu species of catalysts were displayed in Table S2. Thus, the content ratio of Cu₁ to Cu_{NP} of P-Cu₁/Cu_{NP}, M-Cu₁/Cu_{NP} and R-Cu₁/Cu_{NP} were 0.05, 0.25 and 0.39, respectively, which is consistent with our catalyst design expectation.

Electrocatalytic CO₂RR performance

The CO₂RR performance of the as-prepared catalysts were first evaluated by linear sweep voltammetry (LSV) in 5 M KOH aqueous solution

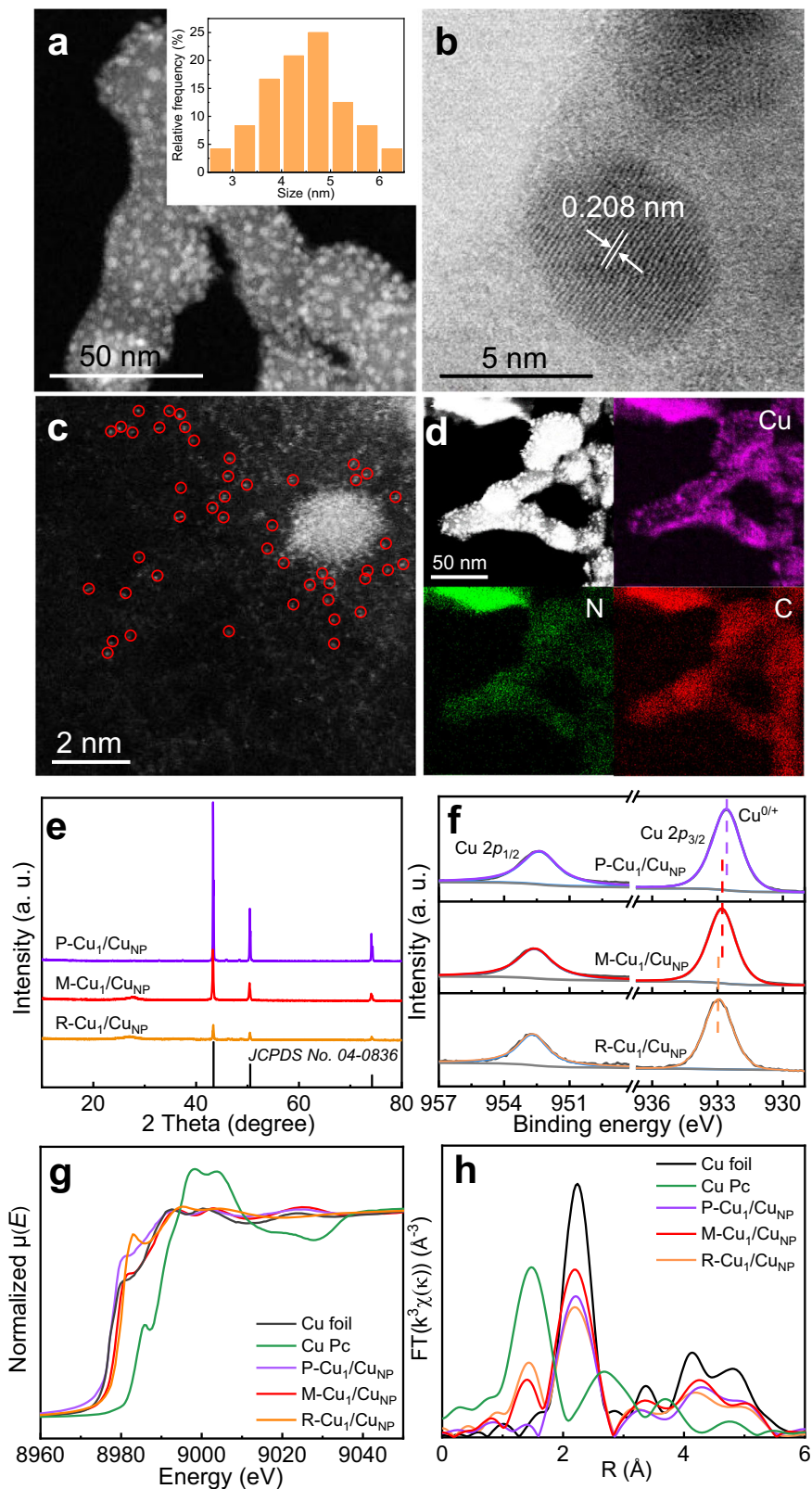


Fig. 1 | Morphology and structure of the catalysts. **a** DF-TEM image (inset shows particle size distribution), **b** HRTEM image, **c** aberration-corrected HAADF-STEM image, and **d** EDS element mappings of M-Cu₁/Cu_{NP}. **e** XRD patterns, **f** XPS spectra

of Cu *2p* orbitals, **g** Cu K-edge XANES spectra, and **h** FT-EXAFS spectra of P-Cu₁/Cu_{NP}, M-Cu₁/Cu_{NP} and, R-Cu₁/Cu_{NP}.

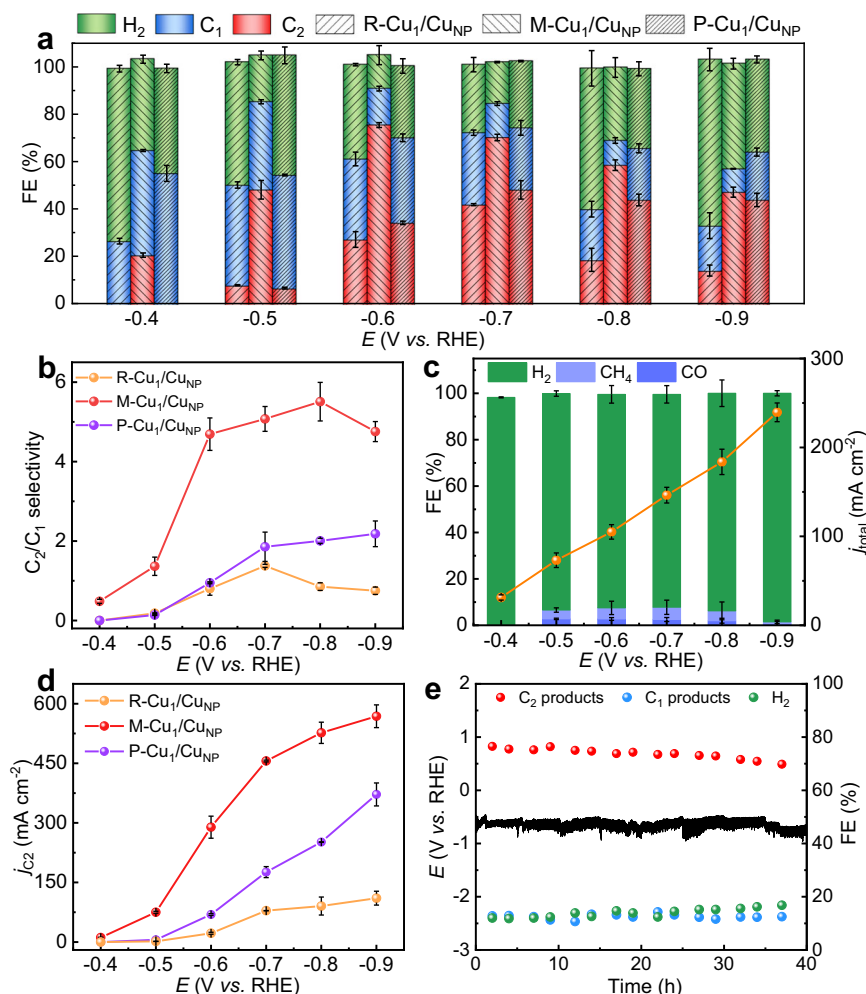


Fig. 2 | CO₂ electroreduction performance. **a** The FEs of C₁ products, C₂ products, H₂, and **b** C₂ and C₁ product selectivity ratio at different potentials over the as-prepared catalysts in 5 M KOH electrolyte. **c** The product FEs and total current density of Cu-N-C at different potentials in 5 M KOH electrolyte. **d** The C₂ partial current density at different potentials over the as-prepared catalysts in 5 M KOH

electrolyte. Values are means and error bars indicate s.d. ($n = 3$ replicates). **e** Long-term stability of M-Cu₁/Cu_{NP} at a constant current density of 400 mA cm⁻² in 5 M KOH electrolyte (the electrode was washed, then dried and the electrolyte was refreshed at intervals 5 h to address the issues of flooding and carbonation).

in a flow cell (Fig. S7). As shown in Fig. S8, all the catalysts exhibited significant increase in cathodic current density when the feed gas was change from N₂ to CO₂, indicating that CO₂RR occurred over R-Cu₁/Cu_{NP}, M-Cu₁/Cu_{NP} and P-Cu₁/Cu_{NP}. Meanwhile, M-Cu₁/Cu_{NP} exhibited the most positive onset potential and highest cathodic current density in the presence of CO₂ gas, and taking -0.8 V as an example, the current density reached up to 1093.0 mA cm⁻² over M-Cu₁/Cu_{NP}, which was roughly 2.5 and 1.7 times higher than that of R-Cu₁/Cu_{NP} and P-Cu₁/Cu_{NP}, respectively. Thus, the results of LSV experiments suggested that M-Cu₁/Cu_{NP} has higher CO₂ activity than R-Cu₁/Cu_{NP} and P-Cu₁/Cu_{NP}, which could be attributed to the moderate content ratio of Cu₁ to Cu_{NP}.

The control potential electrolysis was then performed to analyze the reduction products and the catalyst loading was 1 mg cm⁻² (Fig. S9). The gas-phase and liquid-phase products were analyzed by gas chromatography and ¹H nuclear magnetic resonance spectroscopy, respectively. H₂, CO, CH₄, formate, C₂H₄, ethanol and acetate were formed. Figure 2a shows that the FE of C₂ products (FE_{C2}) of M-Cu₁/Cu_{NP} exhibited a volcano-shaped dependence on the applied potential (Fig. S10, Tables S3–S5), and a maximum FE_{C2} could reach 75.4% at -0.6 V, which is much higher than that over R-Cu₁/Cu_{NP} and P-Cu₁/Cu_{NP}. The maximum FE_{C2} of P-Cu₁/Cu_{NP} was 47.3% at -0.7 V, which closed to the performance of Cu nanoparticles reported in the

literature^{22,27}. Moreover, the M-Cu₁/Cu_{NP} had a lower onset potential for C₂ products formation. The FE_{C2} could reach 20.5% at -0.4 V over M-Cu₁/Cu_{NP}, while C₂ products cannot be detected over R-Cu₁/Cu_{NP} and P-Cu₁/Cu_{NP} under the same potential. The ratio of FE_{C2} to FE_{C1} could keep >4.5 from -0.6 to -0.9 V over M-Cu₁/Cu_{NP}, while those of R-Cu₁/Cu_{NP} and P-Cu₁/Cu_{NP} were below 2 in the whole applied potential range (Fig. 2b). Furthermore, M-Cu₁/Cu_{NP} was treated by sulfuric acid solution to completely remove Cu NPs, resulting in a catalyst denoted as Cu-N-C. The results of TEM, XRD, XPS and XAS indicated that only Cu single atoms existed in the Cu-N-C catalyst (Figs. S11, S12). H₂ was the dominant product over Cu-N-C in the whole applied potentials range, suggesting that the atomic Cu sites mainly facilitated H₂O dissociation (Fig. 2c and Table S6). The formation of CO and CH₄ was also observed, in agreement with previous reports that Cu single atoms could generate H₂, CO, and CH₄^{25,28,29}. These results suggest a dual-active sites effect between Cu sites and Cu NPs, and the proper ratio of Cu₁ to Cu_{NP} would obviously enhance the selectivity for C₂ products.

From FE_{C2} and total current density (Fig. S13), the C₂ products partial current density (j_{C2}) of catalysts at different potentials was obtained and shown in Fig. 2d. It could reach 289.2 mA cm⁻² over M-Cu₁/Cu_{NP} at -0.6 V vs. RHE, exceed by up to 13.1-fold and 4.2-fold than that on R-Cu₁/Cu_{NP} (22.1 mA cm⁻²) and P-Cu₁/Cu_{NP} (69.3 mA cm⁻²), respectively. Besides, a high total current density of 1207.6 mA cm⁻²

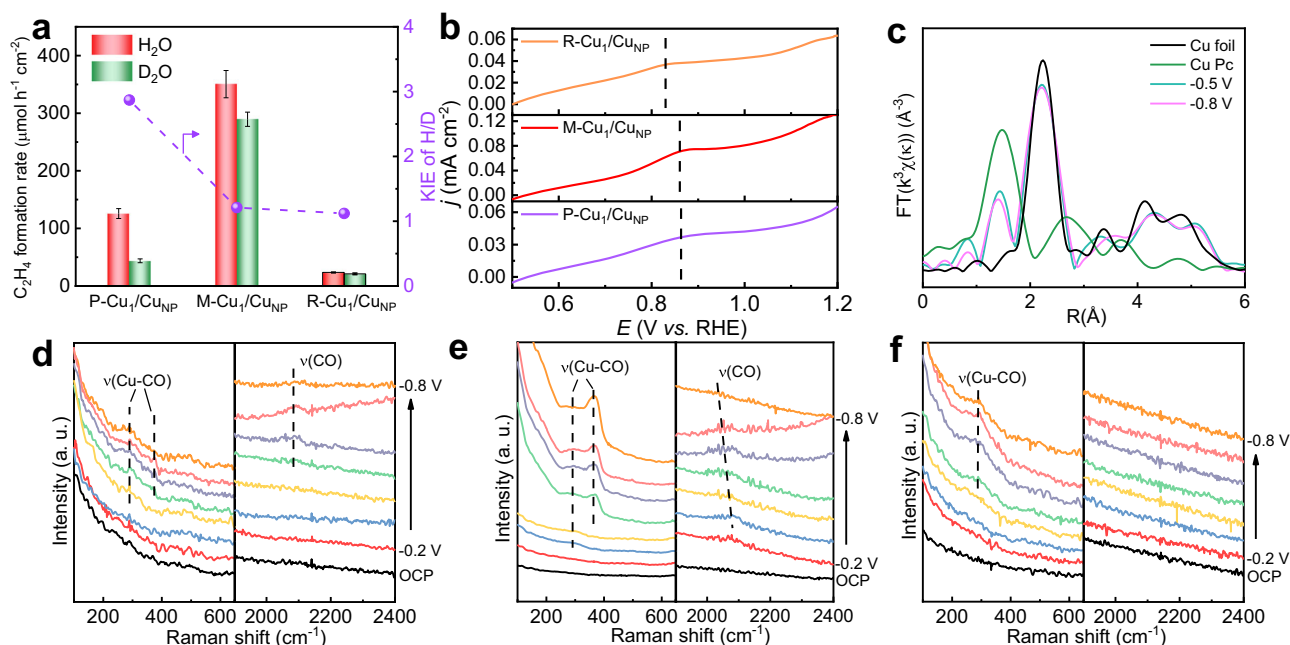


Fig. 3 | The mechanism analysis. **a** The kinetic isotope effect (KIE) of H₂O/D₂O on P-Cu₁/Cu_{NP}, M-Cu₁/Cu_{NP} and R-Cu₁/Cu_{NP} at -0.6 V in flow cell with 5 M KOH electrolyte. **b** The electrochemical CO stripping voltammetry tests of P-Cu₁/Cu_{NP}, M-Cu₁/Cu_{NP} and R-Cu₁/Cu_{NP} in 0.1 M Na₂SO₄ electrolyte. **c** In situ FT EXAFS spectra

at Cu K-edge over M-Cu₁/Cu_{NP} at various potentials in 5 M KOH electrolyte. In situ surface-enhanced Raman spectra recorded at different applied potentials for **(d)** P-Cu₁/Cu_{NP}, **(e)** M-Cu₁/Cu_{NP} and **(f)** R-Cu₁/Cu_{NP} during CO₂RR in 5 M KOH electrolyte.

was obtained at -0.9 V over M-Cu₁/Cu_{NP}, delivering a FE_{C₂} of 47.1% with a partial current density of 568.5 mA cm⁻². We further normalized the j_{C_2} on the basis of the electrochemical active surface area (ECSA), which was measured by the double-layer capacitance (C_{dl}) method (Fig. S14). Even after normalization, M-Cu₁/Cu_{NP} still exhibited the highest normalized j_{C_2} among the catalysts (Fig. S15), confirming that the intrinsic catalytic activity of M-Cu₁/Cu_{NP} is higher than that of P-Cu₁/Cu_{NP} and R-Cu₁/Cu_{NP}. Moreover, we also increased the loading of P-Cu₁/Cu_{NP} and R-Cu₁/Cu_{NP} in accordance with the ECSA results, ensuring the catalytic activity were measured under similar ECSA condition. The results suggested that M-Cu₁/Cu_{NP} maintained the largest C₂ products selectivity and partial current density (Fig. S16), further confirming that the intrinsic catalytic activity of M-Cu₁/Cu_{NP} exceeds that of both P-Cu₁/Cu_{NP} and R-Cu₁/Cu_{NP}. Compared with reported electrocatalysts for CO₂RR to C₂₊ products in the literature, M-Cu₁/Cu_{NP} exhibited higher CO₂RR to C₂₊ products activity at low applied potential, especially in term of C₂₊ partial current density (Table S7).

The long-term stability test was conducted through chronopotentiometry for 40 h and the electrode was washed, then dried and the electrolyte was refreshed at intervals 5 h to address the issues of flooding and carbonation. Fig. 2e and Fig. S17 showed that no obvious change was observed over the potential and products selectivity, the high FE of C₂ products could be hold over 70% on M-Cu₁/Cu_{NP} during the electrolysis. The morphology, valence states and crystal structure of M-Cu₁/Cu_{NP} after 40 h CO₂RR experiment were characterized (Figs. S18, S19). TEM image suggested the size Cu NPs is similar to that before used and the aberration-corrected HAADF-STEM image confirmed that Cu₁ site and Cu NPs still coexisted in M-Cu₁/Cu_{NP}. The Cu LMM Auger spectra show that Cu⁺ and Cu⁰ coexisted in M-Cu₁/Cu_{NP}. Meanwhile, no obvious difference was observed in N 1s XPS spectra between before and after CO₂RR experiment, and only the peaks corresponding to Cu were observed in XRD spectrum after CO₂RR experiment. All these results indicated the excellent stability of the catalyst.

The kinetic isotope effect (KIE) of H₂O/D₂O (H/D) experiments were performed to get insights into the role of H₂O dissociation in

CO₂-to-C₂ products (Fig. 3a). When H₂O was replaced by D₂O in the electrolyte, the formation rate of the product (e.g., C₂H₄) decreased over P-Cu₁/Cu_{NP}, M-Cu₁/Cu_{NP} and R-Cu₁/Cu_{NP}, and the level of decrease closely related to the content ratio of Cu₁/Cu_{NP}. If the KIE value (defined as the ratio of C₂H₄ formation rates in H₂O and D₂O) closes to 1, H₂O dissociation is not the rate-determining step over the catalyst. The KIE values for R-Cu₁/Cu_{NP}, M-Cu₁/Cu_{NP} and P-Cu₁/Cu_{NP} were 1.12, 1.21 and 2.87, respectively, which indicated that H₂O dissociation was accelerated gradually with an increasing Cu₁/Cu_{NP} content ratio. These results confirmed that the atomic Cu sites were responsible for accelerating H₂O dissociation and provided proton to adjacent Cu NPs, thus affecting CO₂-to-C₂ products. Meanwhile, the N-doped carbon matrix catalysts has been reported to favor the migration of proton³⁰. In addition, the H₂ formation rate in 5 M KOH H₂O solution and D₂O solution was presented in Fig. S20. An obvious decrease was observed over all the catalysts, while the decreasing degree followed the sequence of P-Cu₁/Cu_{NP} > M-Cu₁/Cu_{NP} > R-Cu₁/Cu_{NP}, suggesting that the increase of Cu single atom content can reduce the influence of isotope effect on H₂ formation rate.

Furthermore, we studied the influence of electrolyte pH on CO₂RR performance over R-Cu₁/Cu_{NP}, M-Cu₁/Cu_{NP} and P-Cu₁/Cu_{NP}. Three different concentrations of KOH aqueous electrolytes, i.e., 0.1 M, 3 M and 5 M, were employed to adjust the pH environment at the electrode/electrolyte interface. The results in Fig. S21 show that the FE and formation rate of C₂ products increased with the increasing pH value of electrolyte, suggesting that strong basic local environment favored the C₂ products formation. Although CO₂RR activity of M-Cu₁/Cu_{NP} in low concentration KOH electrolytes was lower than that in 5 M KOH electrolyte, M-Cu₁/Cu_{NP} exhibited higher FE and formation rate of C₂ products than P-Cu₁/Cu_{NP} and R-Cu₁/Cu_{NP} in low concentration KOH electrolytes, which suggested that the cooperative effect of Cu NPs and atomic Cu sites still facilitated C₂ products formation. The ratio of C₂ products formation rate over M-Cu₁/Cu_{NP} to P-Cu₁/Cu_{NP}, i.e., Rate_M/Rate_P, in 5 M KOH (3.4) is higher than those in 3 M KOH (3.0) and 0.1 M KOH (2.3). This demonstrated that the role of atomic Cu sites in accelerating the H₂O dissociation process was significantly more

pronounced at higher pH values, leading to the enhanced C₂ products formation, even if the dissociation of H₂O in higher pH electrolyte was a sluggish step.

We then investigated the capacity adsorption and activation of CO₂ and CO molecules on R-Cu₁/Cu_{NP}, M-Cu₁/Cu_{NP} and P-Cu₁/Cu_{NP} via gas electro-response experiments in a self-designed gas adsorption electro-response device (Fig. S22)³¹. The results in Fig. S23 and Fig. S24 show that the CO₂ and CO adsorption responses changed in the sequence of R-Cu₁/Cu_{NP} < M-Cu₁/Cu_{NP} < P-Cu₁/Cu_{NP}, suggesting that the adsorption and activation of CO₂ and CO were promoted as the ratio of Cu₁ to Cu_{NP} decreased. On the other hand, the electrochemical CO stripping voltammetry tests of R-Cu₁/Cu_{NP}, M-Cu₁/Cu_{NP} and P-Cu₁/Cu_{NP} were also performed to study the CO adsorption ability. Figure 3b shows a peak in the potential range of 0.8–0.9 V for all three catalysts. No peak was observed in the LSV curve without CO adsorption (Fig. S25). According to prior literature^{32–34}, the peak at around 0.8–0.9 V can be attributed to the CO stripping peak. Interestingly, the CO stripping peak occurred at around 0.89 V for M-Cu₁/Cu_{NP} and P-Cu₁/Cu_{NP}, while it was around 0.82 V for R-Cu₁/Cu_{NP}. The positive shift suggested that M-Cu₁/Cu_{NP} and P-Cu₁/Cu_{NP} had a stronger CO binding ability than R-Cu₁/Cu_{NP}, which have higher Cu NP content. The results above indicated that the Cu NPs was beneficial for the adsorption and activation of CO₂ and CO.

In situ X-ray absorption spectroscopy (XAS) experiments were performed on M-Cu₁/Cu_{NP} to investigate the changes of Cu valence state and structure during CO₂RR (Fig. S26). In the XANES spectra (Fig. S27), the Cu K-edge adsorption spectra did not show obvious difference under different potentials, indicating that the average Cu valence state kept stable during the reaction. Moreover, the peaks corresponding to Cu-N and Cu-Cu coordination still existed in FT EXAFS spectra (Fig. 3c), with no notable change was observed in peak intensity, suggesting the stability of the content ratio of Cu₁ to Cu_{NP}. The results of in situ XAS experiments showed that the structure and content of Cu₁ and Cu_{NP} remained stable during CO₂RR.

In situ surface-enhanced Raman spectroscopy (SERS) was employed to reveal the interactions between Cu species and the reaction intermediates during CO₂RR (Fig. S28)^{35–38}. As shown in the Raman spectra under different potentials (Fig. 3d–f), the peaks assigned to the restricted rotation of adsorbed CO (298 cm⁻¹, $\nu(\text{Cu-CO})$), Cu-CO stretching (365 cm⁻¹, $\nu(\text{Cu-CO})$) and C-O stretching of atop *CO (2000–2100 cm⁻¹, $\nu(\text{CO})$) were observed from –0.3 to –0.8 V over M-Cu₁/Cu_{NP}. In contrast, the $\nu(\text{Cu-CO})$ and $\nu(\text{CO})$ peaks over P-Cu₁/Cu_{NP} appeared from –0.4 V and –0.5 V, respectively. These observation could be related to the lower onset potential for C₂ products formation over M-Cu₁/Cu_{NP}. Only CO rotation peaks can be observed on R-Cu₁/Cu_{NP} from –0.4 to –0.8 V, meaning poor CO₂ reduction activity. In situ SERS was also conducted over Cu-N-C (Fig. S29), whereas no peaks associated with *CO intermediate were observed, suggesting that single atomic Cu was not conducive to the conversion of CO₂ to adsorbed CO. The results of in situ SERS indicated that CO₂-to-C₂ products proceeded via CO intermediate process and a moderate content ratio of Cu₁ to Cu_{NP} facilitated the conversion of CO₂ to adsorbed CO.

Online differential electrochemical mass spectrometry (DEMS) was conducted to investigate reaction mechanisms (Fig. S30), which extracts volatile intermediates and products generated on the electrode surface into the mass spectrometer within milliseconds, utilizing the pressure difference in a vacuum as the driving force^{39,40}. During five continuous cycles at –0.6 V vs. RHE, the m/z signal of 29 that correspond to CHO could be detected over M-Cu₁/Cu_{NP}, while it was absent in P-Cu₁/Cu_{NP} and R-Cu₁/Cu_{NP} (Fig. S31). The results of online DEMS demonstrated that the crucial role of the proper Cu₁ to Cu_{NP} content ratio in CHO formation. Meanwhile, in situ attenuated total reflection-surface-enhanced IR absorption spectroscopy (ATR-SEIRAS) spectra were further collected to trace the evolution of reaction intermediates

during CO₂RR from –0.2 to –0.9 V over R-Cu₁/Cu_{NP}, M-Cu₁/Cu_{NP} and P-Cu₁/Cu_{NP} (Figs. S32, S33). The peak at around 2100 cm⁻¹ can be attributed to electrogenerated CO adsorbed (*CO) on catalyst surface^{41,42}, which did not appear until the applied potential reached –0.5 V on R-Cu₁/Cu_{NP} and P-Cu₁/Cu_{NP}. However, the $\nu(*\text{CO})$ peak over M-Cu₁/Cu_{NP} obviously existed from –0.3 to –0.9 V and the peak intensity was stronger than that of R-Cu₁/Cu_{NP} and P-Cu₁/Cu_{NP}, suggesting that M-Cu₁/Cu_{NP} preferred to generate *CO intermediate. Meanwhile, a peak at 1748 cm⁻¹ observed over M-Cu₁/Cu_{NP} from –0.3 to –0.9 V can be ascribed to the *CHO intermediate^{12,38,39}, and its change trend was similar to that of *CO intermediate, indicating that the *CHO was originated from the hydrogenation of *CO with the assistance of *H. Nevertheless, the *CHO peak was not observed on R-Cu₁/Cu_{NP} and P-Cu₁/Cu_{NP}, meaning that proper content ratio of Cu₁ to Cu_{NP} is necessary for *CHO formation.

DFT calculations

DFT calculations were performed to gain insights into the CO₂RR mechanism. According to the HRTEM and EXAFS fitting results, the Cu(111) facet and the Cu-N₄ were used as the models of Cu NPs and atomic Cu sites, respectively. All the computational structure models and the detailed data are shown in Figs. S34–S40. We first calculated CO₂ to adsorbed CO (*CO) process to verify if the catalyst is beneficial for CO₂ activation, as *CO is a crucial intermediate for C₂ products formation. The calculations revealed that CO₂ could be converted to *CO via a *COOH intermediate. However, the energy barrier of CO₂-to-*CO over the Cu(111) facet and Cu-N₄ was found to be 0.44 and 1.40 eV, respectively (Fig. 4a and Fig. S35). This indicated that CO₂ preferred to be activated on Cu(111) facet, which is accordance with the experiment results.

In general, the C-C coupling reaction was considered as the rate-determining step for CO₂-to-C₂₊ products^{23,43}. Although CO₂ could be easily converted to *CO on Cu(111) facet, high uphill reaction energy was needed to form *O*CCO intermediate, meaning that the C-C coupling reaction through *CO dimerization is difficult. We further calculated the C-C coupling reaction through different C₁ species (*CO, *CHO, *COH). As shown in Fig. 4b, the uphill reaction energy for the *CHO formation was 0.65 eV lower than that of the *COH formation (1.07 eV). This indicated that the *CO preferred to hydrogenate into *CHO rather than *COH, which is consistent with the ATR-SEIRAS results. Afterwards, both *CHO*CO and *COH*COH coupling were endoergic, while *CHO dimerization to form *OHCCHO* intermediate was exergonic. Therefore, the hydrogenation of *CO into *CHO then coupling of *CHO into *OHCCHO* is the most favorable routes in C-C coupling reaction.

Considering that the *CHO intermediate was originated from the hydrogenation of *CO with the assistance of *H, the influence of *H coverage on *CHO formation over Cu(111) facet were investigated. Our calculations revealed that that increasing the *H coverage on Cu(111) up to 1/4 decreased the reaction energy of *CO hydrogenation to *CHO (Fig. 4c and Fig. S41). However, a further increase of the *H coverage to 1/2 disfavored the formation of *CHO. These findings confirm that a moderate *H coverage facilitated the formation of *CHO, thus promoted the C-C coupling reaction and improved the CO₂-to-C₂ products efficiency. The moderate atomic Cu sites in M-Cu₁/Cu_{NP} can accelerate the H₂O dissociation process in alkaline electrolyte to provide the moderate *H coverage on Cu NP surface (Fig. 4d), therefore, the M-Cu₁/Cu_{NP} exhibited excellent CO₂RR to C₂ products performance.

Discussion

In summary, a series of dual-active sites catalysts with co-loaded Cu NPs and atomic Cu sites on N-doped carbon matrix have been successfully synthesized and evaluated for CO₂ electroreduction. Among them, M-Cu₁/Cu_{NP} exhibited a C₂ products FE of 75.4% with a

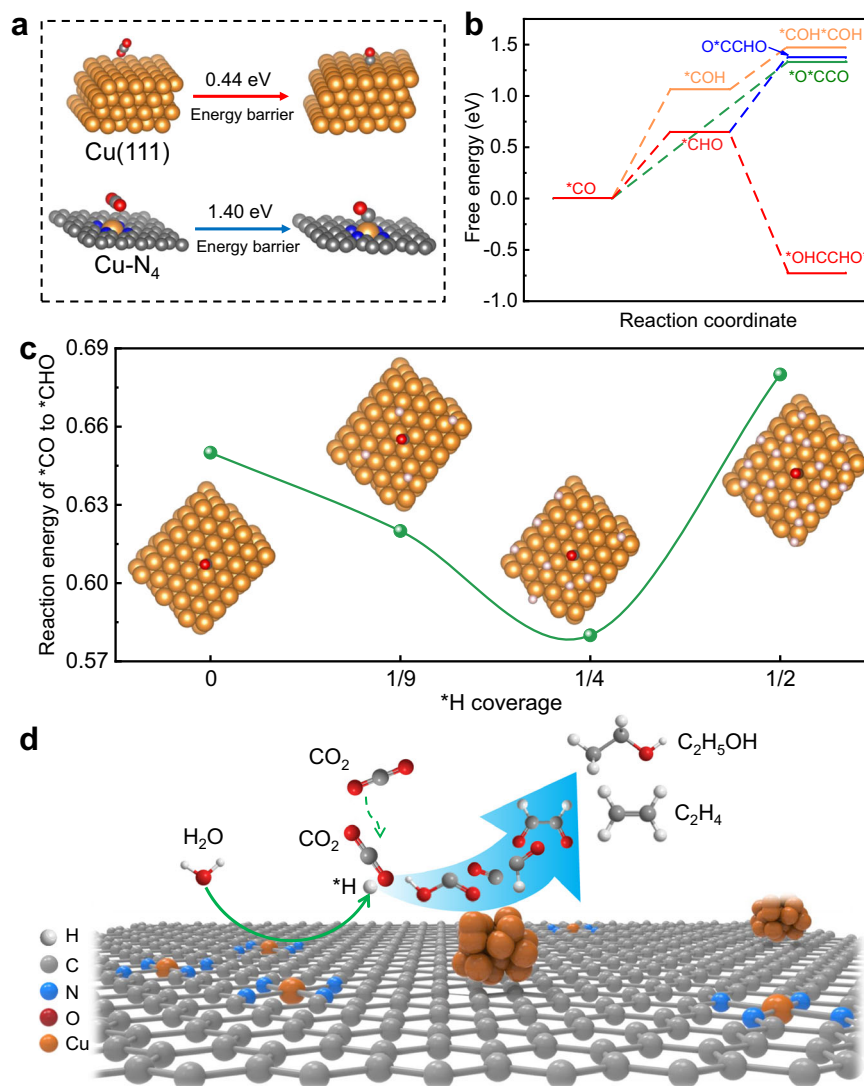


Fig. 4 | The DFT calculations. **a** The energy barrier of CO₂ was converted to *CO over Cu(111) and Cu-N₄. **b** The free energy diagram for the CO₂RR to describe the possible C-C coupling step from *CO over Cu(111). **c** Reaction energy of *CO

hydrogenation to *CHO on Cu(111) as a function of *H coverage. **d** Proposed reaction mechanism for CO₂RR to C₂ products on the M-Cu₁/Cu_{NP}.

corresponding partial current density of 289.2 mA cm⁻² at -0.6 V, as well as remarkable long-term stability. The detailed study revealed that atomic Cu sites could promote H₂O dissociation to provide *H, and the Cu NPs was beneficial for the adsorption and conversion of CO₂. The in situ spectroscopic characterization showed that moderate content ratio of atomic Cu sites to Cu NPs facilitated CO₂ conversion to adsorbed CO, resulting in M-Cu₁/Cu_{NP} possessing a lower onset potential for C₂ products. Furthermore, online DEMS and in situ ATR-SEIRAS revealed the presence of the intermediate *CHO over M-Cu₁/Cu_{NP}, which was originated from the hydrogenation of *CO with the assistance of *H. DFT calculations demonstrated that the C-C coupling step was promoted through *CHO dimerization reaction on Cu NPs, and the moderate *H coverage facilitated the formation of *CHO. Therefore, the excellent catalytic performance of as-fabricated dual-active sites catalyst originated from the dual-active sites effect of atomic Cu sites and Cu NPs. The atomic Cu sites promoted H₂O dissociation to provide *H, which in turn migrated to Cu NPs and facilitated *CO protonation to form *CHO by modulating the *H coverage on Cu NPs, leading to high activity for C₂ products production. This work puts forward rational concept for promoting conversion CO₂ to C₂ products through modulate the adsorbed hydrogen coverage on

Cu-based catalysts. We believe that it will inspire the design of more dual-/multi-active sites catalysts for multi-step reactions.

Methods

Materials

Copper nitrate hydrate (Cu(NO₃)₂·3H₂O, purity > 99%), guanidine thiocyanate (C₂H₆N₄S, purity > 99%), potassium hydroxide (KOH, purity > 85%), potassium bicarbonate (KHCO₃, purity > 99.5%), sodium sulfate (Na₂SO₄, purity > 99%), 2, 2-dimethyl-2-silapentane-5-sulfonate (DSS, 99%), Deuterium oxide (D₂O, purity > 99.9), gas diffusion electrode (YLS-30) with 10% PTFE and microporous layer, anion exchange membrane (FAA-3-PK-130) and Ni foam (purity > 99.8%, thickness 0.5 mm) were purchased from Alfa Aesar China Co., Ltd. CO₂ (99.999%), N₂ (99.999%) and 10% H₂/Ar were provided by Beijing Analytical Instrument Company. All materials were used directly without further purification and all the aqueous solutions were prepared by Milli Q water (18.2 MΩ cm, 298 K).

Catalysts characterization

The morphologies of as-synthesized catalysts were characterized by a JEOL JEM-2100F high-resolution transmission electron microscopy

(HR-TEM). The high-angle annular dark-field scanning transmission electron microscopy (HAADF-STEM) characterization and corresponding energy-dispersive spectroscopy (EDS) were conducted on aberration-corrected JEM-ARM300F operated at 300 kV. Powder X-ray diffraction (XRD) analysis of the samples were performed on the X-ray diffractometer (Model D/MAX2500, Rigaku) with Cu-K α radiation and the scattering range of 2θ was from 5° to 90° , with a scanning rate of 5° min^{-1} . X-ray photoelectron spectroscopy (XPS) analysis was performed on Thermo Fisher Scientific ESCA Lab 250Xi using 200 W monochromatic Al K α (1486.6 eV) radiation under a pressure of 3×10^{-10} mbar, and the binding energy was referenced to the C 1s peak at 284.4 eV. The X-ray absorption data at the Cu K-edge of the catalysts were recorded in transmission mode using ion chambers at the 4B9A beamline of Beijing Synchrotron Radiation Facility (BSRF) and the radiation was monochromatized by a Si (111) double-crystal monochromator. All collected spectra were analyzed using Athena and Artemis program within the IFEFFIT software packages.

Catalyst synthesis

50.8 mmol of guanidine thiocyanate and a quantity of $\text{Cu}(\text{NO}_3)_2 \cdot 3\text{H}_2\text{O}$ were added to a flask containing 50 mL deionized water with vigorously stirring at 80°C . After stirring for 4 h, the temperature was raised to 100°C to evaporated water. The collected solid product was grounded evenly and pyrolyzed at 600°C with $10^\circ\text{C min}^{-1}$ for 3.5 h under N_2 atmosphere, heated at 400°C with 2°C min^{-1} for 2 h under 10% H_2/Ar atmosphere. After cooled down to room temperature, the as-obtained solid was washed with ethanol and deionized water for several times and dried in vacuum at 60°C overnight. Specifically, for R-Cu $_1$ /Cu $_{\text{NP}}$, M-Cu $_1$ /Cu $_{\text{NP}}$, and P-Cu $_1$ /Cu $_{\text{NP}}$, the amount of used $\text{Cu}(\text{NO}_3)_2 \cdot 3\text{H}_2\text{O}$ was 3.81, 6.35 and 8.89 mmol, respectively. For comparison, Cu-N-C was prepared by treating M-Cu $_1$ /Cu $_{\text{NP}}$ with acid treatment. The M-Cu $_1$ /Cu $_{\text{NP}}$ was added into 50 mL 1 M sulfuric acid aqueous solution and heated at 80°C for 48 h, then washed with deionized water several times and dried at 80°C overnight.

Electrocatalytic CO_2 reduction

To prepared gas diffusion electrode, 1 mg catalyst was suspended in 500 μL isopropanol with 10 μL Nafion D-521 dispersion (5 wt%) to form a homogeneous ink. Then the catalyst ink was spread onto the gas diffusion electrode of $0.5 \times 2 \text{ cm}^2$ in area by a micropipette to make sure the mass loading of the catalyst was 1 mg cm^{-2} , and then dried under room temperature. All the electrochemical experiments were conducted on the electrochemical workstation (CHI 660E) equipped with a high current amplifier (CHI 680 C) and the CO_2 RR performance was investigated in flow cell (Fig. S7). The prepared gas diffusion electrode and Ni foam were used as the cathode and anode, respectively. An anion exchange membrane was used to separate the cathode and anode. Aqueous KOH solution (5 M) was used as the electrolyte solution and the electrolyte volume was 30 mL, and the electrolyte volume in the cell is 0.5 mL. The catholyte solution and anolyte solution were recirculated by two pumps with flow rates of 10 mL min^{-1} and 30 mL min^{-1} , respectively. Meanwhile, CO_2 gas was continuously supplied to the gas chamber by using a mass flow controller with a flow rate of 40 mL min^{-1} . All the potentials were measured against a Hg/HgO reference electrode and converted to versus RHE with iR (80%) compensations, i represents the current obtained at corresponding potential, R is ohmic resistance of the cell measured by electrochemical workstation:

$$E_{\text{RHE}} = E_{\text{Hg/HgO}} + 0.098 + 0.059 \times \text{pH} - iR \times 80\% \quad (1)$$

The chronopotentiometry method was used for evaluating long-term activity stability of electrocatalyst in 5 M KOH electrolyte. In order to address the issues of flooding and carbonation accumulation of GDE, the CO_2 RR was interrupted every 5 h and the GDE were removed,

washed with deionized water and followed by dryness under N_2 atmosphere. Meanwhile, the electrolyte solution was refreshed for each interval.

Product analysis

The gaseous products were collected using a gas bag and quantified by gas chromatography (GC 7890B). A thermal conductivity detector (TCD) and a flame ionization detector (FID) were used to quantify H_2 , CO, and other alkane contents, respectively. The Faradaic efficiency (FE) of gaseous products was calculated by the equation:

$$FE = znVF/Q \times 100\% \quad (2)$$

Where z represents the number of electrons transferred for product formation, n is the volume concentration from GC, V is the total volume calculated by outlet flow rate, F is Faraday constant (96485 C/mol) and the Q is the amount of cumulative charge recorded by the electrochemical workstation.

The liquid product was analyzed by ^1H NMR (Bruker Advance III 400 HD spectrometer) in deuterioxide. To accurately integrate the products in NMR analysis, the sodium 2, 2-dimethyl-2-silapentane-5-sulfonate (DSS) was the reference for ethanol and acetic acid, and phenol was the reference for formate. The FE of liquid products was calculated by the equation:

$$FE = znVF/Q \times 100\% \quad (3)$$

Where z represents the number of electrons transferred for product formation, C is the liquid concentration obtained from NMR, V is electrolyte volume, F is Faraday constant (96485 C/mol) and the Q is the amount of cumulative charge recorded by the electrochemical workstation.

Double layer capacitance measurements

The electrochemical active surface area is proportional to double layer capacitance, which measures the capacitive current associated with double-layer charging from the scan-rate dependence of cyclic voltammogram. The double layer capacitance was determined in a single-compartment electrolytic cell with 0.5 M KHCO_3 aqueous solution as electrolyte. Ag/AgCl electrode and graphite rod were used as reference electrode and counter electrode, respectively. The scan rates of cyclic voltammogram were 20, 40, 60, 80, 100 mV s^{-1} .

Gas electro-response experiments

A self-designed gas adsorption electroresponse device (Fig. S19) was used to perform gas electro-response experiments. To prepared the electrode, 5 mg catalyst was suspended in 1 mL isopropanol to form a homogeneous ink. Then the catalyst ink was spread onto the Cu foam with area of $1 \times 2 \text{ cm}^2$ by a micropipette and then dried under room temperature. The as-prepared electrode was put into a sealed container and connected with electrochemical workstation through two electrode system. Before Ar, CO_2 or CO gas was injected into the sealed container, the container was kept in vacuum state by a vacuum pump. Various potentials were applied on the electrode to observed the change of current curve as a function of time under different atmosphere. The adsorption of various gas on the electrode surface would induce the change of current response. Considering the catalyst loading and the size of the Cu foam used in each experiment is the same, the difference of current density under Ar and CO_2 (or CO) atmosphere can reflect the adsorbed capacity of CO_2 (or CO) on the catalyst surface.

CO stripping test

CO stripping experiments were conducted in a single-chamber electrolytic cell with three electrode system through linear sweep voltammetry method. To prepared working electrode, 1 mg catalyst was

suspended in 500 μL isopropanol with 10 μL Nafion D-521 dispersion (5 wt%) to form a homogeneous ink. Then the catalyst ink was spread onto the carbon paper of $1 \times 1 \text{ cm}^2$ in area and then dried under room temperature. Ag/AgCl electrode and graphite rod were used as reference electrode and counter electrode, respectively. The electrolyte was 0.1 M Na_2SO_4 aqueous solution. The CO adsorption procedure was accomplished by polarizing the working electrode at +0.2 V and bubbling the electrolyte with CO for 10 min and subsequently with N_2 for another 10 min. Then the linear sweep voltammetry was conducted from 0.5 to 1.2 V with scan rate of 10 mV s^{-1} .

In situ XAS measurements

A custom-designed flow cell was used to conduct in situ XAS measurements (Fig. S23), the gas diffusion electrode loaded with catalyst (1 mg cm^{-2}), Ni foam and Hg/HgO electrode were chosen as the working electrode, counter electrode and reference electrode, respectively. The 5 M KOH aqueous solution was used as electrolyte and were recirculated by pump with flow rates of 20 mL min^{-1} . CO_2 gas was continuously supplied to the gas chamber with a flow rate of 40 mL min^{-1} . Data were recorded in fluorescence excitation mode using a Lytle detector. During the in situ XAS experiments, the spectrum was recorded following the application of a corresponding potential to the electrode for a duration of 600 s. Beamline of Beijing Synchrotron Radiation Facility (BSRF) and the radiation was monochromatized by a Si (111) double-crystal monochromator. All collected spectra were analyzed using Athena and Artemis program within the IFFFIT software packages.

In situ Raman measurements

A flow cell with a quartz window by GaossUnion (Tianjin) Photoelectric Technology Company was used to carry out in situ Raman measurements using a Horiba LabRAM HR Evolution Raman microscope (Fig. S25). A 785 nm laser was used and signals were recorded using a 20 s integration and by averaging two scans. The gas diffusion electrode sprayed with the catalyst was used as working electrode and a graphite rod and a Hg/HgO electrode were used as counter and reference electrodes, respectively. The counter electrode was separated from the working electrode by anion exchange membrane. The 5 M KOH aqueous solution was used as electrolyte and were recirculated by pump with flow rates of 20 mL min^{-1} . Meanwhile, CO_2 gas was continuously supplied to the gas chamber with a flow rate of 40 mL min^{-1} .

In situ ATR-SEIRAS measurements

The experiments were conducted in a modified electrochemical cell that integrated into a Nicolet 6700 FTIR spectrometer equipped with MCT detector cooled by liquid nitrogen (Fig. S27). The catalysts ink was dropped on a germanium ATR crystal deposited with Au film. A platinum wire and a Hg/HgO electrode were used as counter and reference electrodes. Each spectrum was collected with 32 times with a resolution of 4 cm^{-1} . The CO_2 -saturated 3 M KOH aqueous solution was used as electrolyte to avoid that the germanium ATR crystal was damaged by strong basic electrolyte. The background spectrum was collected at the potential of +0.1 V vs RHE.

Online DEMS measurement

A custom-designed flow cell was used to conduct online DEMS measurements (Fig. S30). The gas diffusion electrode loaded with catalyst, platinum wire and Hg/HgO electrode were chosen as the working electrode, counter electrode, and reference electrode, respectively. The 5 M KOH aqueous solution was used as electrolyte and were recirculated by pump with flow rates of 20 mL min^{-1} . CO_2 gas was continuously supplied to the gas chamber with a flow rate of 40 mL min^{-1} . A potentiostatic test at -0.6 V (vs. RHE) was performed in an alternating manner. Following the completion of each electrochemical test and the return of the mass signal to its baseline level, the subsequent cycle commenced, employing identical experimental

conditions to minimize the possibility of inadvertent errors. The experiment was terminated after the completion of five cycles.

DFT calculations

Density function theory calculation were performed by using the CP2K package⁴⁴. PBE functional⁴⁵ with Grimme D3 correction⁴⁶ was used to describe the system. Unrestricted Kohn-Sham DFT has been used as the electronic structure method in the framework of the Gaussian and plane waves method^{47,48}. The Goedecker-Teter-Hutter (GTH) pseudopotentials^{49,50}, DZVPMOLOPT-GTH basis sets were utilized to describe the molecules. A plane-wave energy cut-off of 500 Ry has been employed. The potential-dependence of reaction free energies in elementary steps involving proton-electron transfers was evaluated using the computational hydrogen electrode (CHE) approach⁵¹.

The Gibbs free energy is calculated using:

$$\Delta G_{\text{free}} = \Delta E_{\text{DFT}} - T\Delta S + \text{ZPE} \quad (4)$$

Where ΔG_{free} is Gibbs free energy, ΔE_{DFT} is energy calculate from DFT, S is entropy, T is temperature (300 K), and ZPE is zero-point energy.

Data availability

The data that support the plots within this paper are available in the Source data file. Additional data available from authors upon request. Source data are provided with this paper.

References

1. Zaera, F. Designing sites in heterogeneous catalysis: Are we reaching selectivities competitive with those of homogeneous catalysts? *Chem. Rev.* **122**, 8594–8757 (2022).
2. Debra, R. R. Catalytic nanoarchitectures—the importance of nothing and the unimportance of periodicity. *Science* **299**, 1698–1701 (2003).
3. Sun, Y. et al. Selective CO_2 photoreduction to CH_4 via Pd^+ -assisted hydrodeoxygenation over CeO_2 nanosheets. *Angew. Chem. Int. Ed.* **61**, e202203249 (2022).
4. Zhao, S. N., Li, J. K., Wang, R., Cai, J. & Zang, S. Q. Electronically and geometrically modified single-atom Fe sites by adjacent Fe NPs for enhanced oxygen reduction. *Adv. Mater.* **34**, 2107291 (2021).
5. Seh, Z. et al. Combining theory and experiment in electrocatalysis: Insights into materials design. *Science* **355**, 146–158 (2017).
6. Li, X., Wang, S., Li, L., Sun, Y. & Xie, Y. Progress and perspective for in situ studies of CO_2 reduction. *J. Am. Chem. Soc.* **142**, 9567–9581 (2020).
7. Chen, Z. et al. In situ carbon encapsulation confined nickel-doped indium oxide nanocrystals for boosting CO_2 electroreduction to the industrial level. *ACS Catal.* **11**, 14596–14604 (2021).
8. Tan, X., Sun, X. & Han, B. Ionic liquid-based electrolytes for CO_2 electroreduction and CO_2 electroorganic transformation. *Natl. Sci. Rev.* **9**, nwab022 (2022).
9. Ren, D., Ang, B. S. H. & Yeo, B. S. Tuning the selectivity of carbon dioxide electroreduction toward ethanol on oxide-derived Cu_xZn catalysts. *ACS Catal.* **6**, 8239–8247 (2016).
10. Seunghwa, L., Gibeom, P. & Jaeyoung, L. Importance of Ag-Cu biphasic boundaries for selective electrochemical reduction of CO_2 to ethanol. *ACS Catal.* **7**, 8594–8604 (2017).
11. Rahaman, M. et al. Selective n-propanol formation from CO_2 over degradation-resistant activated PdCu alloy foam electrocatalysts. *Green. Chem.* **22**, 6497–6509 (2020).
12. Ma, W. et al. Electrocatalytic reduction of CO_2 to ethylene and ethanol through hydrogen-assisted C-C coupling over fluorine-modified copper. *Nat. Catal.* **3**, 478–487 (2020).
13. Luo, M. et al. Hydroxide promoting carbon dioxide electroreduction to ethanol on copper via tuning of adsorbed hydrogen. *Nat. Commun.* **10**, 5814 (2019).

14. Chen, S. et al. Engineering water molecules activation center on multisite electrocatalysts for enhanced CO₂ methanation. *J. Am. Chem. Soc.* **144**, 12807–12815 (2022).
15. Ma, W. et al. Promoting electrocatalytic CO₂ reduction to formate via sulfur-boosting water activation on indium surfaces. *Nat. Commun.* **10**, 892 (2019).
16. Chen, X. et al. Promoting water dissociation for efficient solar driven CO₂ electroreduction via improving hydroxyl adsorption. *Nat. Commun.* **14**, 751 (2023).
17. Staszak-Jirkovsky, J. et al. Design of active and stable Co-Mo-Sx chalcogenides as pH-universal catalysts for the hydrogen evolution reaction. *Nat. Mater.* **15**, 197–203 (2016).
18. Luo, H., Li, B., Ma, J. G. & Cheng, P. Surface modification of nano-Cu₂O for controlling CO₂ electrochemical reduction to ethylene and syngas. *Angew. Chem. Int. Ed.* **61**, e202116736 (2022).
19. Chen, C. et al. Boosting the productivity of electrochemical CO₂ reduction to multi-carbon products by enhancing CO₂ diffusion through porous organic cage. *Angew. Chem. Int. Ed.* **61**, e202202607 (2022).
20. Huang, J. E. et al. CO₂ electrolysis to multicarbon products in strong acid. *Science* **372**, 1074–1078 (2021).
21. Wu, Z. Z. et al. Identification of Cu(100)/Cu(111) interfaces as superior active sites for CO dimerization during CO₂ electroreduction. *J. Am. Chem. Soc.* **144**, 259–269 (2022).
22. Yang, P. P. et al. Protecting copper oxidation state via intermediate confinement for selective CO₂ electroreduction to C₂₊ fuels. *J. Am. Chem. Soc.* **142**, 6400–6408 (2020).
23. Yang, R. et al. In situ halogen-ion leaching regulates multiple sites on tandem catalysts for efficient CO₂ electroreduction to C₂₊ products. *Angew. Chem. Int. Ed.* **61**, e202116706 (2022).
24. Fu, W. et al. Photoinduced loading of electron-rich Cu single atoms by moderate coordination for hydrogen evolution. *Nat. Commun.* **13**, 5496 (2022).
25. Zhang, L. & Zhou, G. Coordination engineering of single-atom copper embedded graphene-like borocarbonitrides for hydrogen production. *Appl. Surf. Sci.* **610**, 155506 (2023).
26. Zhang, W. et al. Synergistic copper nanoparticles and adjacent single atoms on biomass-derived N-doped carbon toward overall water splitting. *Inorg. Chem. Front.* **10**, 443–453 (2023).
27. Rossi, K. & Buonsanti, R. Shaping copper nanocatalysts to steer selectivity in the electrochemical CO₂ reduction reaction. *Acc. Chem. Res.* **55**, 629–637 (2022).
28. Xu, C. et al. Highly selective two-electron electrocatalytic CO₂ reduction on single-atom Cu catalysts. *Small Struct.* **2**, 2000058 (2020).
29. Cai, Y. et al. Insights on forming N,O-coordinated Cu single-atom catalysts for electrochemical reduction CO₂ to methane. *Nat. Commun.* **12**, 586 (2021).
30. Liu, P. et al. Synergy between palladium single atoms and nanoparticles via hydrogen spillover for enhancing CO₂ photoreduction to CH₄. *Adv. Mater.* **34**, 2200057 (2022).
31. Yang, B. et al. Accelerating CO₂ electroreduction to multicarbon products via synergistic electric-thermal field on copper nanoneedles. *J. Am. Chem. Soc.* **144**, 3039–3049 (2022).
32. Guo, W. et al. Highly efficient CO₂ electroreduction to methanol via atomically dispersed Sn coupled with defective CuO catalysts. *Angew. Chem. Int. Ed.* **60**, 21979–21987 (2021).
33. Garg, A. et al. Transition-metal nitride core@noble-metal shell nanoparticles as highly CO tolerant catalysts. *Angew. Chem. Int. Ed.* **56**, 8828–8833 (2017).
34. Zhan, C. et al. Subnanometer high-entropy alloy nanowires enable remarkable hydrogen oxidation catalysis. *Nat. Commun.* **12**, 6261 (2021).
35. Zhao, Y. et al. Speciation of Cu surfaces during the electrochemical CO reduction reaction. *J. Am. Chem. Soc.* **142**, 9735–9743 (2020).
36. Gunathunge, C. M., Ovalle, V. J., Li, Y., Janik, M. J. & Waagele, M. M. Existence of an electrochemically inert CO population on Cu electrodes in alkaline pH. *ACS Catal.* **8**, 7507–7516 (2018).
37. Chang, X. et al. Understanding the complementarities of surface-enhanced infrared and Raman spectroscopies in CO adsorption and electrochemical reduction. *Nat. Commun.* **13**, 2656 (2022).
38. Song, X., Xu, L., Sun, X. & Han, B. In situ/operando characterization techniques for electrochemical CO₂ reduction. *Sci. China Chem.* **66**, 315–323 (2023).
39. Wang, Y., Wang, C., Li, M., Yu, Y. & Zhang, B. Nitrate electroreduction: Mechanism insight, in situ characterization, performance evaluation, and challenges. *Chem. Soc. Rev.* **50**, 6720–6733 (2021).
40. Han, S. et al. Ultralow overpotential nitrate reduction to ammonia via a three-step relay mechanism. *Nat. Catal.* **6**, 402–414 (2023).
41. Deng, B. et al. Crystal plane is not the key factor for CO₂-to-methane electrosynthesis on reconstructed Cu₂O microparticles. *Angew. Chem. Int. Ed.* **61**, e202114080 (2021).
42. Wei, X. et al. Highly selective reduction of CO₂ to C₂₊ hydrocarbons at Cu/polyaniline interfaces. *ACS Catal.* **10**, 4103–4111 (2020).
43. Wang, P. et al. Boosting electrocatalytic CO₂-to-ethanol production via asymmetric C-C coupling. *Nat. Commun.* **13**, 3754 (2022).
44. Hutter, J., Iannuzzi, M., Schiffmann, F. & VandeVondele, J. CP2K: Atomistic simulations of condensed matter systems. *Wires Comput. Mol. Sci.* **4**, 15–25 (2014).
45. Perdew, J. P., Burke, K. & Ernzerhof, M. Generalized gradient approximation made simple (vol 77, pg 3865, 1996). *Phys. Rev. Lett.* **78**, 1396–1396 (1997).
46. Grimme, S. Semiempirical GGA-type density functional constructed with a long-range dispersion correction. *J. Comput. Chem.* **27**, 1787–1799 (2006).
47. Vandevondele, J. & Hutter, J. Gaussian basis sets for accurate calculations on molecular systems in gas and condensed phases. *J. Chem. Phys.* **127**, 114105 (2007).
48. Vandevondele, J. et al. QUICKSTEP: Fast and accurate density functional calculations using a mixed Gaussian and plane waves approach. *Comput. Phys. Commun.* **167**, 103–128 (2005).
49. Goedecker, S., Teter, M. & Hutter, J. Separable dual-space Gaussian pseudopotentials. *Phys. Rev. B* **54**, 1703–1710 (1996).
50. Hartwigsen, C., Goedecker, S. & Hutter, J. Relativistic separable dual-space Gaussian pseudopotentials from H to Rn. *Phys. Rev. B* **58**, 3641–3662 (1998).
51. Norskov, J. K. et al. Origin of the overpotential for oxygen reduction at a fuel-cell cathode. *J. Phys. Chem. B* **108**, 17886–17892 (2004).

Acknowledgements

The work was supported by National Natural Science Foundation of China (22203099, 22002172, 22033009, 21890761, 22121002), Beijing Natural Science Foundation (J210020), China Postdoctoral Science Foundation (2022M713200), S&T Program of Hebei (B2021208074), and Photon Science Center for Carbon Neutrality. The X-ray absorption spectroscopy measurements were performed at Beamline 4B9A at Beijing Synchrotron Radiation Facility (BSRF).

Author contributions

J.F., X.S., and B.H. proposed the project, designed the experiments, and wrote the manuscript; J.F. performed the whole experiments; S.L. assisted in analysing the experimental data; L.Z., L.X., X.M., X.T. and L.W. conducted a part of characterizations. Q.Q., T.W., and J.Z. participated in discussions. X.S. and B.H. supervised the whole project.

Competing interests

The authors declare no competing interests.

Additional information

Supplementary information The online version contains supplementary material available at <https://doi.org/10.1038/s41467-023-40412-9>.

Correspondence and requests for materials should be addressed to Xiaofu Sun or Buxing Han.

Peer review information *Nature Communications* thanks Min-Rui Gao and the other, anonymous, reviewers for their contribution to the peer review of this work. A peer review file is available.

Reprints and permissions information is available at <http://www.nature.com/reprints>

Publisher's note Springer Nature remains neutral with regard to jurisdictional claims in published maps and institutional affiliations.

Open Access This article is licensed under a Creative Commons Attribution 4.0 International License, which permits use, sharing, adaptation, distribution and reproduction in any medium or format, as long as you give appropriate credit to the original author(s) and the source, provide a link to the Creative Commons licence, and indicate if changes were made. The images or other third party material in this article are included in the article's Creative Commons licence, unless indicated otherwise in a credit line to the material. If material is not included in the article's Creative Commons licence and your intended use is not permitted by statutory regulation or exceeds the permitted use, you will need to obtain permission directly from the copyright holder. To view a copy of this licence, visit <http://creativecommons.org/licenses/by/4.0/>.

© The Author(s) 2023